Article | Received 3 November 2025; Revised 23 December 2025; Accepted 23 December 2025; Published 12 January 2026
https://doi.org/10.55092/am20260002

Effect of WC content on microstructure and properties of Ni60/WC composite coatings for railway couplers

Xinlin Wang, Guiwei Liu, Meichao Qin*, Xiaochi Wang and Shuangxin Zhao

School of Mechanical Engineering, Dalian Jiaotong University, Dalian 116028, Liaoning, China

* Correspondence author; E-mail: qmcdalian@126.com.

Highlights:

- WC content controls Ni60/WC coating microstructure and performance.
- Peak hardness (1099 HV) achieved at 50% WC, 5.5 × higher than substrate.
- Optimal wear resistance at 30% WC, with friction coefficient stable near 0.2.
- Best corrosion resistance observed at low WC content (10%).
- 30% WC balances crack sensitivity, hardness, wear/corrosion resistance for coupler repair.

Abstract: Due to corrosion erosion and mechanical wear, the coupler connecting surface needs to be frequently polished and repaired. In order to avoid the fact that the fit clearance of the connecting surface gradually exceeds the design standard limit due to multiple maintenance, the coupler parts are scrapped in advance due to performance failure. In this research, Ni60/WC composite coatings were deposited onto 18MnNiV coupler substrate, with their geometric morphology, metallographic characteristics, microhardness, and corrosion resistance, and friction resistance systematically characterized. The influence of WC content (10%–60%) on the microstructure and properties of the coatings was thoroughly investigated. The findings indicate that the overall performance of the cladding layer can be markedly enhanced through the incorporation of WC particles. In terms of microstructure, the cladding layer with low WC content (10%–20%) takes γ-(Fe, Ni) as the matrix, WC particles are dispersed, the microstructure presents typical dendritic characteristics, and the surface quality is good. In terms of mechanical properties, the hardness of the cladding layer reaches a peak value of 1099 HV when the WC content is 50%, which is 5.5 times higher than that of the matrix (about 200 HV). At a tungsten carbide (WC) content of 30%, the cladding layer exhibits optimal wear resistance, with a wear loss measured at merely 0.170g (6.5% lower than that of 60% WC), the friction coefficient is stable at about 0.2, and the predominant wear mechanism is slight abrasive wear. At a tungsten carbide (WC) content of 10%, the cladding layer exhibits the highest corrosion potential and the lowest corrosion current density, and the corrosion resistance is the best.

Keywords: laser cladding; Ni60/WC; current assistance; mixed powder; coupler

1. Introduction

Laser cladding technology, as an emerging advanced repair method, is applied to restore the couplers, which are the core components of railway vehicles and undertake multiple critical tasks such as connection, traction, and buffering. During train operation, the coupling surface will be damaged by metal corrosion, friction wear, *etc.* [1]. The traditional methods for repairing vehicle couplings include welding and spraying, but these methods have many drawbacks. For example, in the welding process, due to the high heat input, deformation and cracks are prone to occur. Moreover, the bonding force between the coating formed by the spraying process and the base material is relatively weak. When subjected to loads, erosion, *etc.*, the coating is very likely to peel off and fail. As an advanced repair technique, laser cladding utilizes a laser beam to rapidly melt the repair material, forming a metallurgical bond with the coupler substrate and resulting in a cladding layer with excellent wear, corrosion, and fatigue resistance [2–4].Compared with traditional repair techniques, the heat affected zone of laser cladding is extremely small, the dilution rate is low, the coating prepared has fine and dense structure, and has high bonding performance with the substrate. This ensures the stability of the repair quality. Consequently, laser cladding technology has garnered increasing research interest for coupler repair [5].

The choice of cladding materials critically influences the quality of the deposited coating. Commonly used cladding materials include self-fluxing alloy powders (Ni-based, Fe-based, Co-based, *etc.*), high-entropy alloy powders, and composite powders [6]. Ni60 is a Ni-based self-melting alloy powder, which possesses excellent corrosion resistance, oxidation resistance and high-temperature resistance. The alloy contains a considerable amount of Cr and B elements, which can respectively exert solid solution strengthening and grain boundary strengthening effects, thereby enhancing the hardness of the cladding layer. It has unique advantages in repair applications [7–9]. However, in scenarios such as coupler repair where hardness and wear resistance requirements are particularly high, a simple Ni-based cladding layer is insufficient to meet the usage needs of the parts. Scholars have adopted some auxiliary processes to enhance the performance characteristics of the nickel-based coating. Among them, the electric field, due to its non-contact nature and the ability to precisely control, demonstrates unique application potential in the field of laser cladding [10]. Wang *et al.* [11] demonstrated through follow-up feed pulsed current-assisted laser cladding technology that pulsed current parameters have a minor effect on dilution rate, with their primary contribution lying in improving the microstructure of the clad layer and suppressing cracks. Yu [12] conducted experiments by adding pulse current to assist laser cladding, aiming to enhance the performance of the steel rail material and obtain steel rail workpieces with fewer defects and excellent performance. Research shows that the introduction of an electric field can significantly optimize the microstructure of the cladding layer, increase density, and effectively suppress the occurrence of defects such as pores and cracks.

Scholars have made certain progress in laser cladding repair under pulsed current, but there are still challenges in material selection and process optimization. To further enhance the performance of the Ni-based coating assisted by current cladding, adding hardness ceramic phases to the Ni-based alloy powder is an effective method [13]. WC is a common ceramic material with excellent ceramic reinforcing phases, featuring extremely high hardness and wear resistance [14]. The incorporation of WC markedly improves the performance characteristics of Ni60 coatings, resulting in a more uniform, dense microstructure with reduced surface defects, thereby hindering the penetration of corrosive media. The

Ni60 matrix provides good toughness, corrosion resistance, and oxidation resistance, which compensates for the inherent low toughness of WC. Furthermore, the self-fluxing and good wetting characteristics of Ni60 promote the uniform distribution of WC particles and ensure strong interfacial bonding with the substrate, crucial for coating quality [15]. Huang *et al.* [16] conducted a study examining the influence of WC content on the microstructural characteristics and mechanical properties of TiC-Ni_3Al metal ceramics. The study revealed that as WC content increased, TiC grains became finer, with their edges bonded by a hard phase and Ni_3Al. At WC contents of 20% and 25%, the coating's toughness and hardness reached their respective peaks. Li *et al.* [17] deposited Ni60/WC composite powder on the QT500-7 surface and found that adding an appropriate amount of WC could enhance the mechanical properties such as hardness and wear resistance of the deposited layer. Hu *et al.* [18] deposited Ni60/WC composite coatings of different mass fractions on stainless steel surfaces and found that as the WC content increased, the grains became finer, and the hardness and mechanical stability of the deposited layer also increased. However, the corrosion rate showed a phenomenon of increasing first and then decreasing. Wang *et al.* [19]. studied the Ni60A/WC in-situ reinforced composite coating and found that the increase in WC content promoted the formation of the in-situ reinforcing body and played a role in fine-grain strengthening, thus increasing the microhardness of the coating. Cui *et al.* [20]. respectively prepared Ni60 alloy coatings and WC-TiO_2/Ni60 composite coatings. The results showed that the microstructure grains in the WC-TiO_2/Ni60 composite coating were more refined, and the hardness and wear resistance were better.

However, studies on the influence of WC content on the performance of current-assisted Ni-based coatings remain scarce. To address this gap, this study investigates the effect of WC content (10%–60%) on Ni60/WC composite coatings fabricated via current-assisted laser multi-pass cladding. The coatings were systematically characterized and analyzed in terms of their macroscopic morphology, phase composition, microstructure, microhardness, and corrosion resistance.

2. Experimental section

2.1. Experimental materials and methods

The substrate employed in this study was 18MnNiV steel, with dimensions of 120 mm × 60 mm × 20 mm. The cladding materials were Ni60 alloy powder and WC powder, which were blended in varying ratios via ball milling to form composite powders. The chemical compositions of the 18MnNiV steel and Ni60 powder are shown in Table 1.

Table 1. Chemical composition of 18MnNiV steel and Ni60 powder (wt %).

Element	Ni	C	Fe	Si	Mn	P	V	B	Cr
18MnNiV	0.3–0.5	0.17–0.22	-	0.2–0.6	0.9–1.2	≤ 0.3	0.13–0.17	-	-
Ni60	Margin	0.8	≤ 5.0	4.0	-	-	-	4.0	16.0

The Ni60/WC composite coating was fabricated on the substrate surface by using the laser cladding process. The Ni60 and WC powders were first weighed according to the desired ratios, placed in a grinding jar, and mixed with grinding balls at a ball-to-powder mass ratio of 10:1. For example, if the total powder mass is 100 g, the grinding ball mass should be 1000 g. The powder was ball-milled at a speed of 500 r/min for 10 hours. Then, it was transferred to the vacuum drying oven and dried at 100 °C for 30 minutes to obtain the mixed powder of Ni60 and WC. The mixed powders were prepared with WC mass fractions ranging from 10 to 60 wt %. Under these process parameters, a single-layer multi-pass Ni60/WC cladding layer was prepared. Before conducting the laser cladding experiment, the substrate surface was polished and rust removed using sandpaper, and then cleaned with absolute ethanol to ensure the surface cleanliness. The LMD 4000-100 type laser was used for laser cladding treatment on the surface of 18MnNiV steel. The experiment was equipped with the G22 series programmable DC pulse power supply, and the electrical parameters were set up before the experiment. The relevant process parameters are shown in Table 2. The connection principle of the equipment is shown in Figure 1.

Table 2. Experimental process parameters.

Process parameters	Parameter values
laser power (W)	1600
scanning speed (mm/s)	4
powder feeding rate (g/min)	1.3
Spot Radius (mm)	3
Carrier Flow (L/min)	10
overlapping ratio (%)	50
pulsed current magnitude (A)	10.1
Pulse current duty cycle (%)	50
Pulse current frequency (Hz)	3000

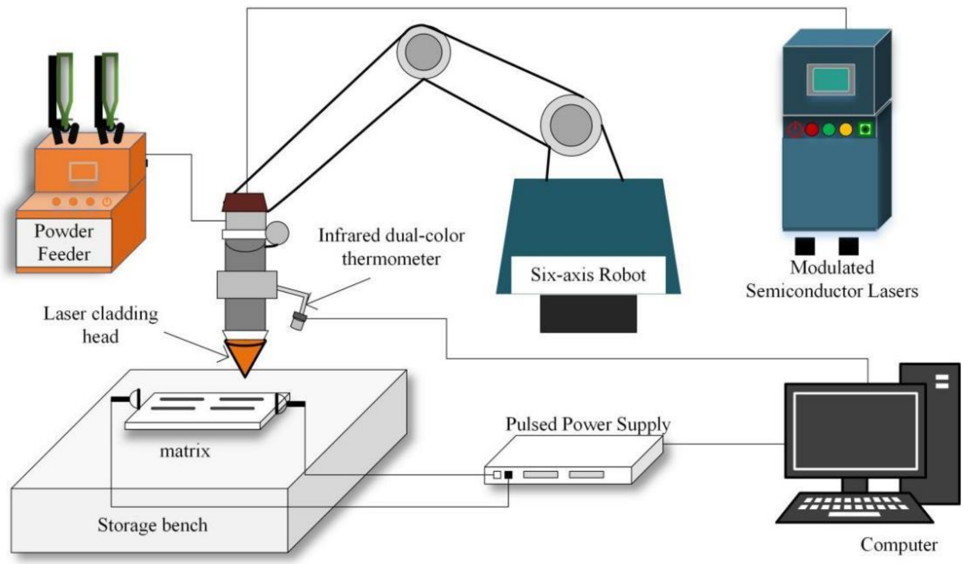

Figure 1. Schematic diagram of experimental equipment for laser cladding of couplers.

Using an electric spark wire cutting machine (DK450, large iron, Guangdong, China), the coated samples were cut into rectangular specimens with dimensions of 35 mm × 10 mm × 10 mm. Water must be continuously added during cutting to prevent the sample from overheating and to avoid thermal alteration of the tissue. To facilitate subsequent grinding and polishing operations, the sample must be embedded in resin material. Pour the liquid embedding material into the mold at room temperature and allow it to cure naturally. The specimens were successively polished after being progressively ground with sandpapers of different grit sizes (from coarse to fine); the specimens were then etched with a saturated oxalic acid solution at a voltage of 5 V for about 50 seconds. After the etching process, the surface of the specimens was cleaned with clean water and anhydrous ethanol in sequence, ready for performance testing.

2.2. Property characterization

Phase analysis of the deposited coating was conducted on an Empyrean Panaco X-ray diffractometer (Malvern Panalytical, Netherlands). The test parameters were set as follows: an accelerating voltage of 40 kV, a tube current of 40 mA, a scanning rate of 4° per minute, a step size of 0.02°, and a diffraction angle range spanning from 0° to 100°.The microstructural characteristics of the cladding layer were examined using a Leica DMi8 metallographic microscope, produced by Leica Microsystems, Germany. The microhardness of the cladding layer and the substrate was tested using the HV-1000 type microhardness tester. The experiment employed a square pyramidal diamond indenter, which was pressed vertically into the surface of the tested material under a specified load. After maintaining the load for a set duration, the load was released. The hardness value was calculated based on the functional relationship between load and indentation size by measuring the diagonal length of the indentation. To obtain the microhardness distribution across the longitudinal and transverse sections of the formed specimens, measurements were taken along the longitudinal path at 10 points spaced 0.1 mm apart and along the transverse path at 3 points spaced 2.5 mm apart. The loading force was 1000 g, the holding time was 15 seconds, and multiple measurements were taken to obtain the average value. The schematic diagram of the measurement position is shown in Figure 2. Wear resistance testing of clad layers was conducted using the CETRUMT multifunctional testing system. The test employed low-speed linear reciprocating point contact friction motion with an applied load of 40 N, a sliding speed of 8 mm/s, and a wear duration of 20 minutes. All environmental conditions were maintained at room temperature under dry conditions. Corrosion resistance testing was conducted using an electrochemical workstation. A 3.5 wt % sodium chloride solution served as the corrosive medium. The electrochemical setup utilized the test specimen as the working electrode, a saturated calomel electrode (SCE) as the reference, and a platinum mesh as the counter electrode. All measurements were performed with a potential scan rate of 10 mV/s. For each WC content (10%–60%), three parallel specimens were prepared. Multiple measurements of hardness, wear volume, and electrochemical parameters were taken, and the average values were recorded.

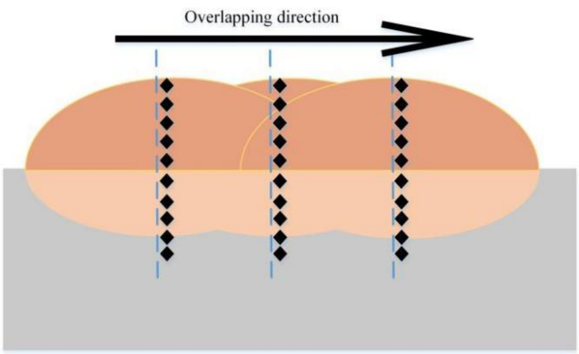

Figure 2. Schematic diagram of measurement positions.

3. Results and discussion

3.1. Macroscopic morphological analysis

Figure 3 presents the surface crack inspection results for the six WC/Ni60 composite coatings, obtained using the DC magnetic particle method. The results reveal a clear trend: coatings with WC content ≤ 20% were crack-free, exhibiting low surface roughness and presumably low thermal stress. In contrast, a significant increase in crack density was observed at WC contents ≥ 30%, with severe transverse through-cracks forming at 50%–60% WC.

This is attributed to the lower proportion of WC phase resulting in a smaller difference in thermal expansion coefficients between the clad layer and the substrate. The resulting lower thermal stresses reduce the tendency for cracking. However, when the WC content exceeds 20%, the difference in thermal expansion coefficients between the WC phase and the metallic substrate significantly increases. This leads to a deterioration in interfacial wettability and bonding properties, intensifying the thermal stresses generated during cooling and becoming the primary driving force for crack initiation. On the other hand, under the high-energy beam of laser cladding, locally overheated WC particles at high concentrations (≥ 30%) undergo decomposition reactions, generating W_2C and free carbon. Free carbon reacts with atmospheric oxygen to form CO and CO_2 gases. These gases, unable to escape the melt pool promptly, create porosity defects within the coating. Porosity acts as a stress concentration point, not only causing localized embrittlement but also providing a preferred path for crack propagation. This synergistic effect is particularly pronounced in coatings with 50%–60% WC content, leading to the formation of macroscopic through cracks.

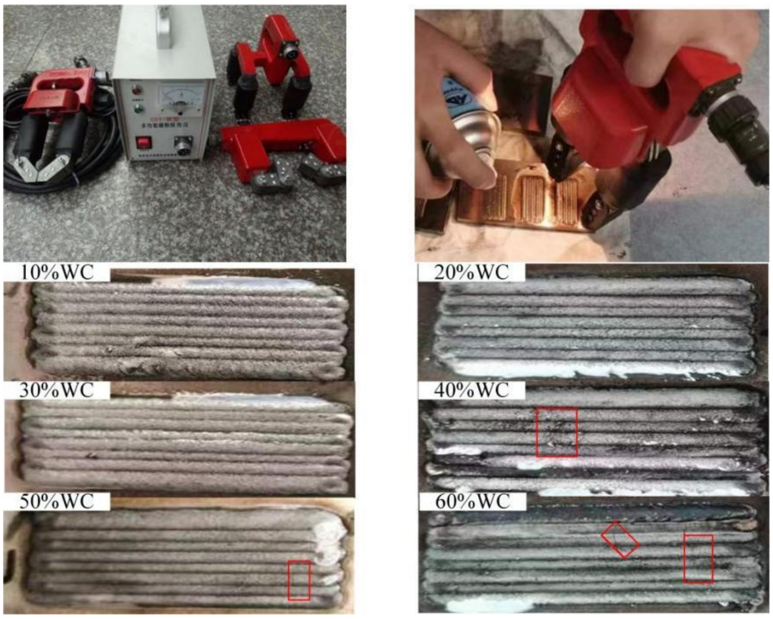

Figure 3. DC flaw detection instrument, operation, and flaw detection results.

3.2. XRD phase detection results

Figure 4 presents the XRD pattern of the Ni60/WC cladding layer. The phase composition of the cladding layer with different WC content is consistent, mainly including γ-(Fe, Ni), $M_{23}C_6$, M_7C_3, WC, W_2C, W_2B_5, *etc.* As the proportion of WC powder increases, the heat input state of the molten pool changes, resulting in a decrease in the content of W_2C due to high temperature decomposition, and the formation of carbides such as $M_{23}C_6$ and M_7C_3 shows an upward trend. The W and C elements produced by the decomposition interact with the matrix alloy elements to form hard phases such as WC, W_2C, W_2B_5, M_7C_3 and $M_{23}C_6$, which become the main contributors to the matrix strengthening of the cladding layer. The cladding layer consists of a γ-(Fe, Ni) solid solution exhibiting a face-centered cubic crystal structure, which serves as the matrix phase, which endows the coating with excellent corrosion resistance. Among them, WC and W_2C achieve grain refinement strengthening effect by refining microstructure, hindering dislocation movement and grain boundary migration [21]. M_7C_3 and $M_{23}C_6$ carbides exist in the matrix in the form of dispersion distribution, which can improve the grain boundary bonding strength, reduce the corrosion medium erosion, and significantly enhance the hardness and corrosion resistance of the cladding layer.

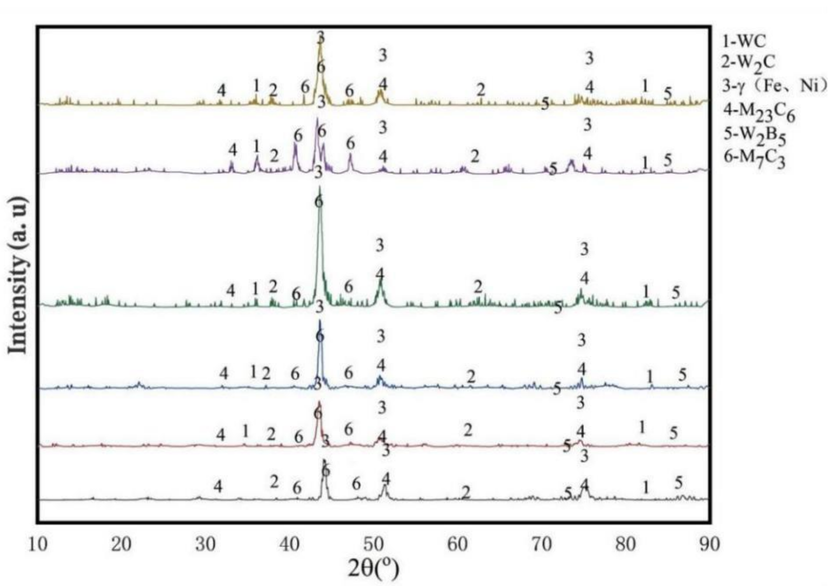

Figure 4. X-ray diffraction (XRD) pattern of the cladding layer alternative options depending on context.

3.3. Microstructure analysis

3.3.1. Microstructure of 10%–20% WC cladding layer

The microstructure of the cladding layer can be clearly divided from bottom to top into the heat-affected zone, the metallurgical bonding zone and the cladding zone. Its structural schematic is shown in Figure 5. The cladding zone is established through the solidification of the cladding powder subsequent to its melting induced by laser irradiation. Its microstructure morphology is mainly regulated by the ratio of the temperature gradient G and the solidification rate R during the solidification stage of the molten pool. As shown in Figure 6, near the fusion line, a high G/R value promotes the directional growth of crystals along the heat dissipation direction, forming planar crystals; as it extends towards the surface of the cladding layer, the G/R value gradually decreases, and the crystal growth mode transitions from cellular crystals to columnar crystals, and finally equiaxed crystals are formed on the surface layer.

As shown in Figure 7, Figure 7a,b depicts the cross-sectional microstructures of 10% WC and 20% WC clad layers, respectively. Microscopic observation reveals that the clad layers exhibit a dendritic structure with well-defined main dendrites and secondary dendrite arms growing in specific directions.

This phenomenon arises from directional solidification driven by fast cooling and temperature gradients during the laser cladding process. As shown in Figure 7c,d within the dense matrix structure, blocky WC phases of varying sizes and concentrations are distributed. Concurrently, needle-like or short rod-shaped high-melting-point compounds, rich in W and Cr elements, are visible. The formation of these compounds is presumed to result from metallurgical reactions between W and Cr in the Ni60 powder and the WC particles.

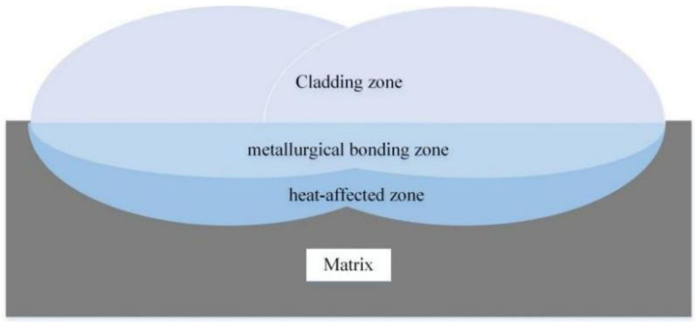

Figure 5. Cross-sectional structure of the cladding layer.

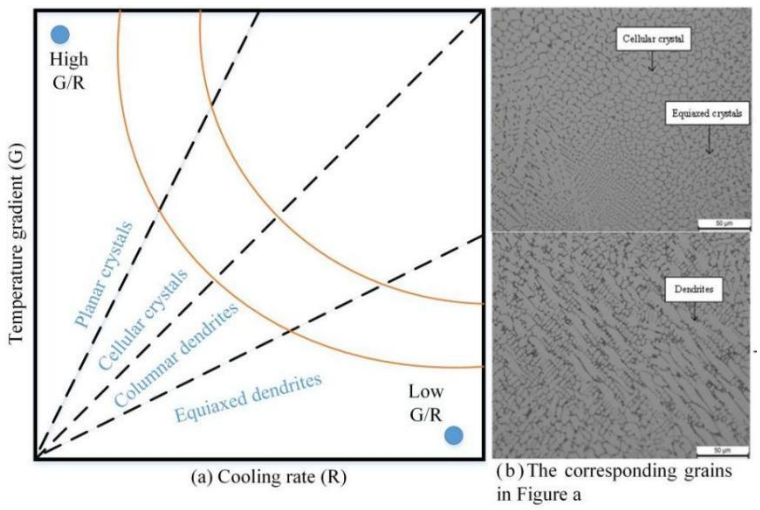

Figure 6. Temperature gradient curve and grain schematic diagram. **(a)** Effect of thermal gradient and cooling rate on grain growth during solidification; **(b)** The corresponding grains in Figure (a).

The addition of WC particles produces a significant grain refinement strengthening effect on the clad layer. As high-hardness, high-rigidity second-phase particles, WC effectively suppresses abnormal grain growth during solidification, promoting a finer grain structure in the composite layer. This fine-grained microstructure enhances material properties through two mechanisms: First, the refinement of grains significantly enhances the quantity of grain boundaries, where lattice distortion and dislocation pile-up significantly boost strength and hardness; Second, the dense network of grain boundaries creates complex diffusion pathways that effectively block the migration of corrosive anions such as Cl^- and SO_4^{2-}, thereby enhancing the coating's barrier properties [22]. Thus, WC particles synergistically strengthen both the corrosion resistance and mechanical properties of the Ni60/WC composite cladding layer by refining grain size and increasing grain boundary density.

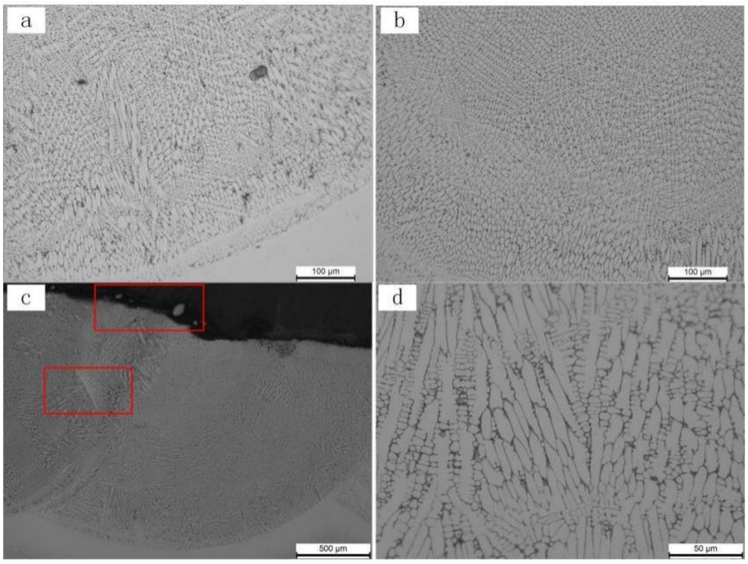

Figure 7. Microstructure diagrams of the cladding layers with 10% and 20% WC content. **(a)** 10%—WC; **(b)** 20%—WC; **(c)** Bulk WC phase; **(d)** Local amplification of needle-like compounds.

3.3.2. Microstructure of 30%–40% WC cladding layer

As shown in Figure 8, where Figure 8a,b are 30% WC and 40% WC cladding layer section organization diagram, with the increase of WC mass fraction, its distribution state gradually changes from uniform dispersion to local aggregation. It can be seen under the microscope that WC particle enrichment zones are formed in some areas. The dendrite structure of Ni60 matrix phase is inhibited to a certain extent, and the dendrite becomes short and the growth direction is relatively messy. This phenomenon occurs due to the presence of a substantial quantity of WC particles, which alters the solidification process of the molten pool. On one hand, WC particles serve as heterogeneous nucleation sites, thereby facilitating nucleation and enhancing the nucleation rate. On the other hand, the disparity in thermophysical properties between WC particles and the Ni60 matrix induces increased thermal stress and compositional segregation during solidification, which affects the normal growth of matrix phase [23]. This structural change further improves the hardness of the cladding layer, but at the same time, it has a certain negative impact on the toughness, resulting in a complex change trend in the comprehensive mechanical properties of the cladding layer.

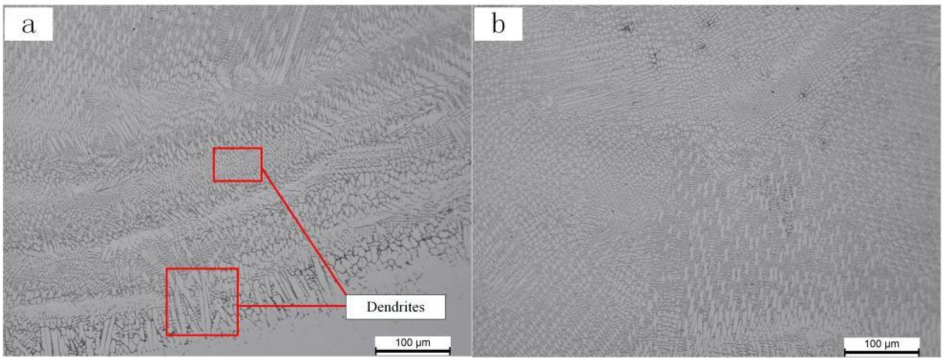

Figure 8. Microstructure diagrams of the cladding layers with 30% and 40% WC content. **(a)** 30%—WC; **(b)** 40%—WC.

3.3.3. Microstructure of 50%–60% WC cladding layer

As shown in Figure 9, where Figure 9a,b depicts cross-sectional microstructures of 50% WC and 60% WC clad layers, respectively, when the WC mass fraction reaches 50% or higher, interconnected WC particles in the upper and middle regions of the clad layer form continuous or semi-continuous network structures. The Ni60 matrix phase fills the spaces between the WC network as fine blocky or strip-like structures. As shown in Figure 9c, WC particles aggregate at the bottom of the cladding layer, dominating the microstructure. In Figure 9d, cracks are visible. Overheating causes WC particles to readily decompose, forming W_2C and free graphite carbon. Without protective gas during the cladding process, graphite carbon rapidly reacts with atmospheric oxygen at high temperatures, producing CO and CO_2 gases. If these gases cannot escape the molten pool promptly, they form porosity defects within the clad layer. Increased porosity causes localized embrittlement, accelerating crack initiation and propagation. At this stage, the clad layer exhibits extremely high hardness. However, due to the continuous WC network structure, cracks readily initiate and propagate along the interfaces between WC particles [24]. This significantly reduces the clad layer's toughness while increasing its brittleness. Such properties are highly detrimental to the impact resistance of the coupler during actual use, making the clad layer prone to spalling or fracture when subjected to substantial impact forces.

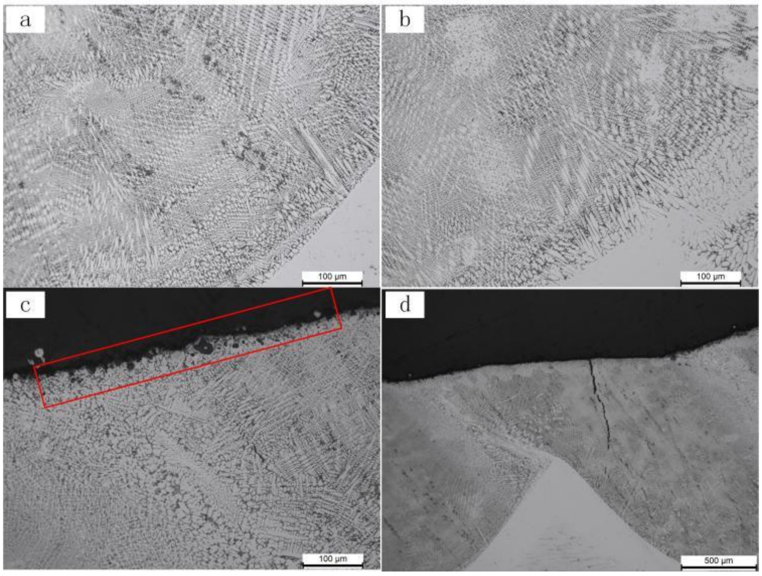

Figure 9. Microstructure diagrams of the cladding layers with 50% and 60% WC content. **(a)** 50%—WC; **(b)** 60%—WC; **(c)** 50%—WC Localized Magnification; **(d)** Crack.

3.4. Microhardness analysis

Figure 10 shows the microhardness distribution curves at different distances from the cladding layer surface. To ensure data reliability, each test point was tested three times at different locations, with the average value calculated. The error in microhardness was controlled within ± 3%, and the error range was marked with error bars. It is evident that the hardness of the cladding layer decreases gradually from the surface toward the substrate. The substrate hardness remains stable with no significant fluctuations. A sharp increase in hardness occurs at the substrate-cladding interface, primarily attributed to the solid solution strengthening of the Ni60 substrate (containing Ni-Cr-B-Si alloy) and the strengthening effect of WC particles.

When the WC mass fraction increases to 50%, the average microhardness of the cladding layer reaches its peak, achieving a 5.5-fold increase compared to the substrate and a 3/7 increase over the 10% WC/Ni60 cladding layer. This is attributed to the enhanced dissolution of WC particles as their content increases. At 60% WC content, the high WC concentration inhibits the fluidity of the Ni60 substrate, leading to the retention of unfused WC particles. Beyond this point, hardness values cease to increase or even decline due to particle agglomeration and coating cracking issues. Significant local hardness variations and instability were observed. XRD phase analysis revealed hard phases such as W_2C and Fe_3W_3C in the 10% WC/Ni60 cladding layer. The relative content of these hard phases gradually increased with rising WC mass fraction. As the number of secondary hard phases within the cladding layer significantly increased, the synergistic effect of grain refinement strengthening and dispersion strengthening intensified, leading to a marked improvement in microhardness.

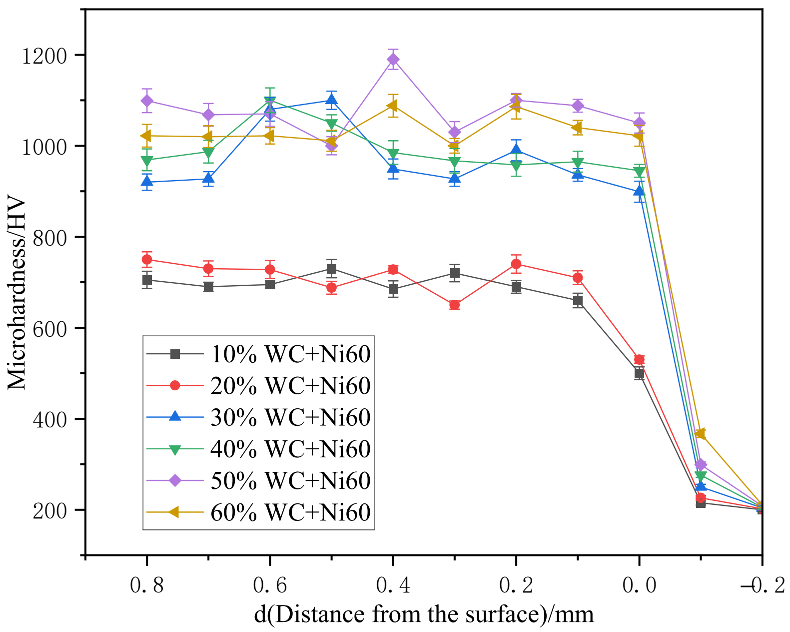

Figure 10. Comparison of the microhardness of the cladding layers under different WC proportions.

Figure 11 shows the average microhardness maps of six nickel-based clad layers. The microhardness values of the clad layers initially exhibited an increase followed by a decrease as the mass fraction of WC was progressively elevated. The average microhardness difference between the 10% WC and 20% WC clad layers was not significant. This was primarily attributed to the relatively insufficient addition of WC particles at these concentrations, which failed to fully exert the dispersion strengthening effect, resulting in a minor improvement in the average microhardness of the clad layers. As the WC mass fraction increased to 30%, the microhardness of the cladding layer significantly improved compared to the preceding groups, indicating that an appropriate amount of WC particles can effectively refine grains and strengthen grain boundaries. When the WC mass fraction reached 50%, the average microhardness of the cladding layer peaked. However, at 60% WC content, WC particle agglomeration began to occur within the coating, accompanied by crack formation and a subsequent decrease in hardness. This occurs because WC particle addition significantly refines the cladding grain size up to 50% WC content. During laser cladding, WC particles thermally decompose into W and C elements, reacting with surrounding Fe, Cr, and other elements to form high-hardness phases such as $Cr_{23}C_6$ and Fe_3W_3C. These hard phases effectively inhibit grain growth and promote microstructural refinement. Simultaneously, partially melted WC particles and in-situ precipitated hard phases are uniformly distributed within the cladding layer [25]. The combined influence of grain refinement strengthening and dispersion strengthening synergistically contributes to the enhancement of the microhardness of the cladding layer.

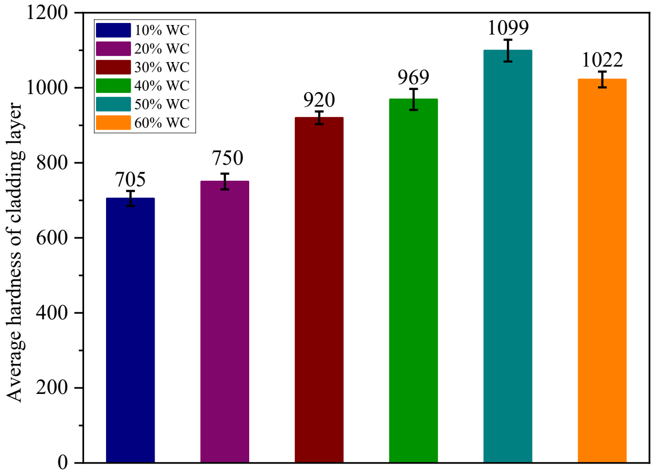

Figure 11. The average surface hardness of the cladding layers with different WC proportions.

3.5. Wear properties

Figure 12 shows the friction coefficient variation curve. It can be observed that the 30% WC cladding layer gradually stabilizes at around 0.2 after varying break-in periods. In contrast, the 40%–60% WC cladding layers exhibit relatively longer break-in periods, with friction coefficient curves fluctuating significantly between 0.4 and 0.5, indicating instability. Comparative analysis indicates that the tribological performance of the 30% WC coating is superior to that of the 40%–60% WC coatings. This advantage is primarily attributed to the absence of defects such as pores in its microstructure, coupled with a more uniform and dense microstructure compared to the latter coatings.

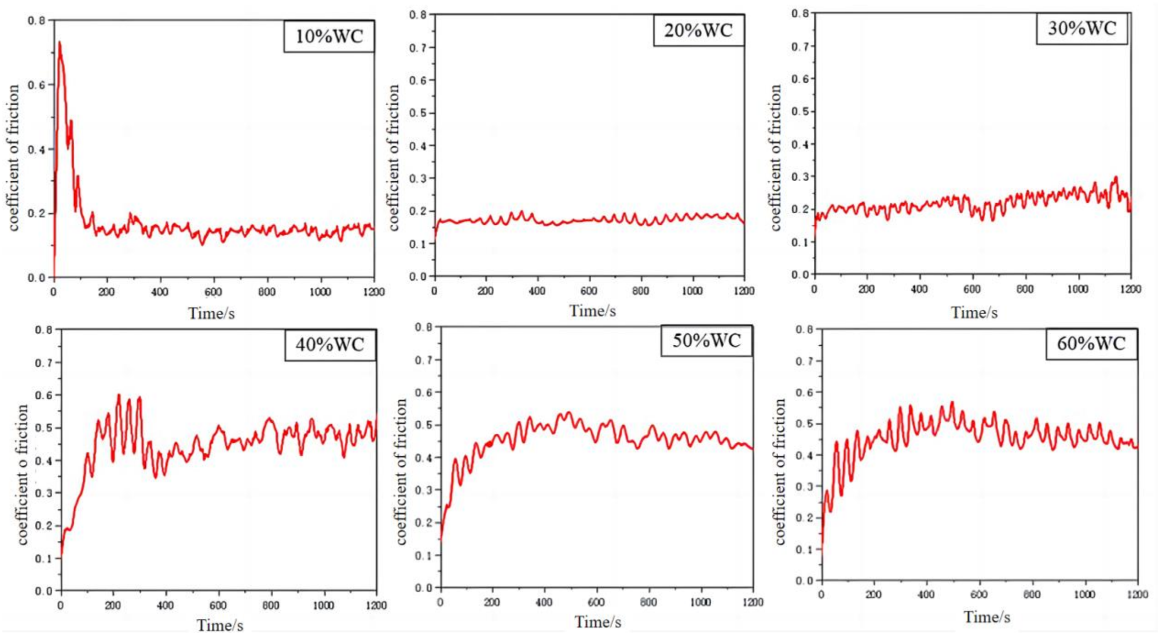

Figure 12. Friction coefficient—Time curves for different WC contents.

The measured masses of the six cladding specimens before and after friction wear testing, along with the mass differences before and after testing, are shown in Table 3. After 20 minutes of wear testing, the wear mass of the 30% WC cladding layer was less than 0.175 g, while that of the 60% WC cladding layer was greater than or equal to 0.175 g. This indicates that the 30% WC cladding layer exhibits superior friction wear resistance compared to the 60% WC cladding layer. The mass loss observed for the coating containing 30% WC was 0.17 g, whereas the coating with 60% WC content exhibited a mass loss of 0.1812 g. These results suggest that the coating with 30% WC demonstrates superior wear resistance.

Table 3. Mass before and after experiment and mass differences.

WC content	Pre-experiment matrix mass(g)	Post-experiment matrix mass(g)	Mass difference of the matrix(g)
10%	32.1454	32.9721	0.1733
20%	32.7110	32.5408	0.1702
30%	32.6567	33.4867	0.1700
40%	31.9251	31.7501	0.1750
50%	32.7016	32.5258	0.1758
60%	32.3977	32.2165	0.1812

When the WC content is $\leq$ 30%, the hard phases within the clad layer exhibit a dispersed distribution as WC increases, significantly enhancing microhardness and effectively suppressing surface adhesive wear behavior. Simultaneously, the inherently low friction characteristics of the hard phases cause the overall friction coefficient of the clad layer to decrease markedly. However, the difference in wear between the 30% WC and 20% WC coatings was not significant. This may be because microcracks began to form in the cladding layer when the WC content reached 30%. The negative cracking effect partially offset the theoretical improvement in wear resistance brought about by the increased WC content, resulting in minimal variation in wear rates. However, when the WC content exceeds 30%, the friction coefficient shows an increasing trend. This is because excessive WC leads to an increase in the variety and complexity of the morphology of the precipitated hard phases within the cladding layer. This is accompanied by grain coarsening, which significantly reduces the toughness of the cladding layer. Consequently, surface cracks and spalling occur, disrupting the surface flatness and ultimately causing the friction coefficient to rise. Combined with microhardness analysis, when the WC mass fraction is low, the increase in microhardness is limited, while the cladding exhibits relatively high toughness. Consequently, as wear progresses, the surface hardened layer is rapidly abraded. Under contact stress, adhesive wear occurs, intensifying the adhesive wear behavior [26,27]. The friction coefficient gradually increases and eventually stabilizes around 0.5.

Experimental results indicate that the 30% WC cladding layer exhibits optimal wear resistance, with its core mechanism stemming from the moderate dissolution and uniform distribution of WC particles within the molten pool. During the rapid solidification process of laser cladding, WC particles at this concentration fully participate in metallurgical reactions, forming uniformly distributed strengthening phases (such as WSi_2, NiW, Fe_6W_6C, *etc.*). These phases reduce friction within the coating, lowering its coefficient of friction and wear rate, thereby effectively enhancing wear resistance.

Figure 13 illustrates the microscopic morphology of wear scars as observed through a microscope. The surface appears relatively rough, exhibiting deep grooves parallel to the sliding direction. The scars also display distinct flake-like features and debris, alongside white particles. This indicates that the wear mechanism of the WC-Ni60 cladding layer involves both abrasive wear and adhesive wear. Ni60 and WC cladding layers with different mass fractions may exhibit distinct wear mechanisms during friction and wear. Cladding layers with low WC content primarily demonstrate adhesive wear and abrasive wear, whereas those with high WC content suffer more severe wear due to particle spalling and crack propagation.

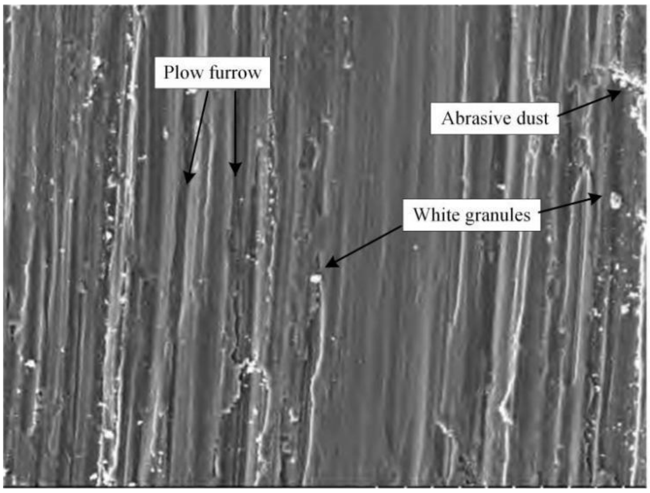

Figure 13. Wear morphology of the coating.

3.6. Electrochemical corrosion analysis

Figure 14 shows the polarization Tafel curves of the Ni60/WC cladding layer in a 3.5% NaCl solution. The self-corrosion potential (Ecorr) serves as the core parameter for assessing the corrosion susceptibility of the cladding layer; a more positive value indicates a lower likelihood of corrosion. The self-corrosion current density (Icorr) serves as an indicator of the corrosion rate of the material, wherein a lower Icorr value signifies a reduced rate of corrosion. No passivation region was observed in the polarization curves of any coating. This is attributed to the incorporation of WC, which fixes Cr elements within carbides (e.g., Cr_3C_2). Consequently, the substrate exhibits insufficient Cr content in the solid solution phase, preventing the formation of a self-healing passivation film.

Analysis of the polarization curve reveals a systematic variation in the Ecorr of the WC/Ni60 coating. Sample S1 exhibits the highest Ecorr, with the remaining samples shifting progressively to the left. Sample S1 exhibits the lowest auto Icorr, while S3's Icorr is lower than S4's, indicating superior corrosion resistance compared to S4. Overall, the corrosion resistance ranking of the first three samples is S1 ≥ S2 ≥ S3, with relatively minor differences. When the WC content exceeds 40%, the corrosion resistance of the cladding layer decreases. This is because elements such as Cr, Ni, and Si in Ni60 enhance the matrix electrode potential through solid solution strengthening, reducing the number of microcells and thereby improving corrosion resistance. Among these, Cr also promotes the formation of a dense and stable Cr_2O_3 passivation film on the steel surface, effectively slowing down the corrosion process. However, with an increase in the mass fraction of WC, there is a corresponding rise in the quantity of unfused WC particles, leading to an increase in microcell formation. Simultaneously, the diffusion of molten W and C atoms creates C-enriched zones, promoting the precipitation of Cr-rich carbides (e.g., $Cr_{23}C_6$). This further depletes Cr in the solid solution, reducing Cr content near grain boundaries and lowering electrode potential, thereby exacerbating intergranular corrosion [28].

Although Ni enhances the material's corrosion resistance by expanding the γ-phase region to form a single-phase austenite, thereby elevating the self-corrosion potential, its positive effects cannot offset the detrimental impact of Cr depletion and microstructural defects caused by excessive WC content.

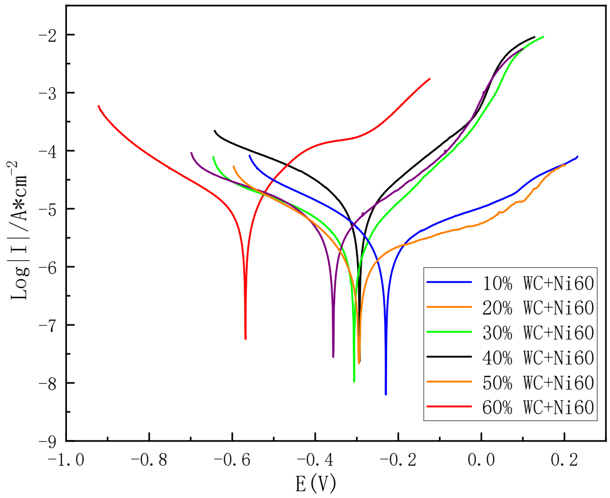

Figure 14. Tafel polarization curves.

4. Conclusions

This research utilized laser cladding technology to apply Ni60/WC composite coatings onto the surface of 18MnNiV steel. The effects of varying WC content (10%–60%) on the microstructure and properties of the clad layers were investigated, yielding the following conclusions:

(1) Microstructural evolution: At low WC content (10%–20%), the cladding layer exhibits a dendritic microstructure with γ-(Fe,Ni) as the matrix and uniformly dispersed WC particles. At medium WC content (30%–40%), WC particles form localized network structures, accompanied by hard phases such as W_2C and M_7C_3, and partial fragmentation of dendrites. At high WC content (50%–60%), the WC phase forms a continuous network accompanied by numerous unmelted WC particles and cracks.

(2) Mechanical Properties: Hardness increases initially then decreases with WC content, peaking at 1099 HV at 50% WC-a 5.5-fold increase over the base material. Wear resistance is optimal at 30% WC, with wear volume reaching only 0.170 g. Wear is predominantly abrasive, yielding a friction coefficient of approximately 0.2. At high WC content (> 40%), increased brittle phases cause a shift to abrasive-adhesive combined wear, with the coefficient of friction fluctuating to 0.4–0.5.

(3) Corrosion Performance: The cladding layer containing 10% tungsten carbide demonstrates the highest corrosion resistance. When the WC content exceeds 30%, chromium elements become immobilized by carbides, leading to reduced passivation film repair capability and a significant increase in pitting corrosion susceptibility.

(4) Overall, the WC content should be maintained around 30%. Within this range, the cladding layer achieves a balance of low crack sensitivity, high hardness, and excellent wear and corrosion resistance, rendering it appropriate for engineering applications, including the repair of couplers.

Data availability statement

No new data were created or analyzed in this study.

Authors' contribution

Conceptualization, Xinlin Wang; methodology, Guiwei Liu; validation, Shuangxin Zhao and Xinlin Wang; formal analysis, Guiwei Liu and Shuangxin Zhao; investigation, Xinlin Wang and Guiwei Liu; resources, Xiaochi Wang; data curation, Shuangxin Zhao; writing—original draft preparation, Xinlin Wang; writing—review and editing, Meichao Qin; visualization, Guiwei Liu; supervision, Xiaochi Wang; project administration, Xinlin Wang. All authors have read and agreed to the published version of the manuscript.

Conflicts of interests

The authors declare no conflict of interest.

References

[1] Sun B, Gao H, Kang H, Liu X, Zhang B. Research on laser cladding repair process for close-coupled couplers of EMUs (In Chinese). *Rail Transit Equip. Technol.*2022, 5:22–24.
[2] Xiao M, Fan Z. Research status and development prospect of extreme high-speed laser cladding technology (In Chinese). *Powder Metall. Mater. Sci. Eng.* 2024, 29(3):151–161.
[3] Zhou H, Wang Y, Wang X, Zhan J, Zhang J. Influence of the coupler and buffer device on the train collision safety. *Proc. Inst. Mech. Eng., Part F: J. Rail Rapid Transit* 2023, 237(3):385–393.
[4] Guo S. Study on laser repairability of surface indentation and scratch defects of SUS301L stainless steel (In Chinese). Master's Thesis, Jilin University, 2024.
[5] Zhang S, Wang J, Zhang G, Fan H. Research status and development trend of alloy coatings prepared by laser cladding technology (In Chinese). *Shanghai Met.* 2025, 47(5):1–6.
[6] Ding R, Wang X, Hu C, Zheng J. Research status of laser cladding technology material system (In Chinese). *Hot Working Process* 2025, 54(20):1–9.
[7] Wang F, Li X, Peng J, Feng X, Liu Z. Investigation of the effect of lap ratio on the microstructure and properties of laser cladding Ni60 coatings (In Chinese). *Laser Appl.* 2025, 45(4):48–57.
[8] Qi X, Li F, Li Y, Gao S, Niu J, *et al.* Regulating the microstructure, wear and corrosion resistance of laser cladded Ni-based composite coating enhanced by in-situ TiC-TiB_2 through heat treatment (In Chinese). *China Surf. Eng.* 2025.
[9] Sun Y, Qin J, Zhang L, Jing P, Liu S, *et al.* Forming behavior and microstructural analysis of Ni60 laser cladding coatings (In Chinese). *Electric Weld. Mach.*2024, 54(11):44–49.
[10] Liu Z, Liu P, Zhou L, Wang L. Effects of pulsed current on the microstructure and properties of laser cladded TC17 titanium alloy. *Materials* 2023, 17(1):91.
[11] Wang D, Zhu Y, Qu G, Zhou X. Research on dilution of laser cladding assisted by pulsed current based on orthogonal experiment. *J. Phys. Conf. Ser.* 2021, 1965(1):012087.
[12] Yu Y. Research on rail laser cladding based on pulse current and temperature detection assistance (In Chinese). Master's Thesis, Dalian Jiaotong University, 2023.
[13] Huang J, Zhu Z, Shi W, Zhao Y, Jiao T, *et al.* Microstructure and properties analysis of Ni60-based/WC composite coatings prepared by laser cladding. *Heliyon* 2024, 10(2):e24494.

[14] Chen S, Wang H, Huang X, Qin S, Hu X. Study on the microstructure and performance of the multi-field composite-assisted laser cladding of nickel-based tungsten carbide coatings. *Metals* 2024, 14(10):1188–1188.
[15] Sun S, Wang J, Xu J, Cheng X, Jing C, *et al.* Preparing WC-Ni coatings with laser cladding technology: A review. *Mater. Today Commun.* 2023, 37:106939.
[16] Huang B, Xiong W, Yao Z, Chen S, Zhang M, *et al.* Effect of WC content on microstructure and mechanical properties of Ni 3 Al-bonded cermets. *Ceram. Int.* 2016, 42(4):5291–5298.
[17] Li W, Yang X, Xiao J, Hou Q. Effect of WC mass fraction on the microstructure and friction properties of WC/Ni60 laser cladding layer of brake discs. *Ceram. Int.* 2021, 47(20):28754–28763.
[18] Hu Y, Wang Z, Pang M. Effect of WC content on laser cladding Ni-based coating on the surface of stainless steel. *Mater. Today Commun.* 2022, 31:103357.
[19] Wang H, Liu K, Li J, Geng S, Jing L, *et al.* Reinforcements/matrix micro-interface evolution and properties of in-situ Ni60A/WC coatings prepared by laser cladding. *Surf. Coat. Technol.* 2024, 484:130834.
[20] Cui C, Guo Y, Wang C, Cheng Y. Microstructure and properties of laser cladding Ni60/WC-TiO_2 composite coatings (In Chinese). *Mater. Eng.* 2025.
[21] Guo H, Liu C, Wang M, Gu B, Wang Y, *et al.* Study on performance of laser cladding of 60 wt %WC-Ni coating with ultrasonic/temperature composite energy field. *J. Alloys Compd.* 2025, 1034:181344–181344.
[22] Li Z. Process optimization and performance study of laser cladding Ni60/WC composite coating on 35CrMoV surface (In Chinese). Master's Thesis, Chongqing Technology and Business University, 2024.
[23] Liu G, Su Y, Xin S, Li C, Deng Z, *et al.* Enhanced wear resistance of Ti reinforced Inconel 718 superalloy manufactured by laser directed energy deposition. *Mater. Charact.* 2024, 209:113736.
[24] Fan S. Study on laser cladding Ni60-WC composite coating technology and erosion wear properties of Q345 steel (In Chinese). Master's Thesis, Henan Polytechnic University, 2023.
[25] Lu H, Shui J, Wang K, Shang Y, Jiang H, *et al.* Effects of dissolving and precipitating of WC particles on performance of Ni60 coating (In Chinese). *Surf. Technol.* 2023, 52(3):189–196.
[26] Liu Y, Wang Q, Xie J, Yang X, Peng P, *et al.* Enhanced surface composite coating on Ti811 alloy by laser cladding towards improved nano-hardness. *Ceram. Int.* 2022, 48(13):18773–18783.
[27] Liu G, Su Y, Pi X, Xin S, Li K, *et al.* Achieving high strength 316L stainless steel by laser directed energy deposition-ultrasonic rolling hybrid process. *Mater. Sci. Eng.: A* 2024, 903:146665.
[28] Xiao Q, Sun W, Liu J, Huang H. Surface corrosion behavior of Ni60A/WC laser cladding coating (In Chinese). *Mater. Rev.* 2021, 35(8):8146–8150.